



UNIVERSITY OF LEEDS

This is a repository copy of *Understanding the emplacement of Martian volcanic rocks using petrofabrics of the nakhlite meteorites*.

White Rose Research Online URL for this paper:
<http://eprints.whiterose.ac.uk/146962/>

Version: Accepted Version

Article:

Daly, L, Piazzolo, S orcid.org/0000-0001-7723-8170, Lee, MR et al. (8 more authors) (2019) Understanding the emplacement of Martian volcanic rocks using petrofabrics of the nakhlite meteorites. *Earth and Planetary Science Letters*, 520. pp. 220-230. ISSN 1385-013X

<https://doi.org/10.1016/j.epsl.2019.05.050>

Reuse

This article is distributed under the terms of the Creative Commons Attribution-NonCommercial-NoDerivs (CC BY-NC-ND) licence. This licence only allows you to download this work and share it with others as long as you credit the authors, but you can't change the article in any way or use it commercially. More information and the full terms of the licence here: <https://creativecommons.org/licenses/>

Takedown

If you consider content in White Rose Research Online to be in breach of UK law, please notify us by emailing eprints@whiterose.ac.uk including the URL of the record and the reason for the withdrawal request.



eprints@whiterose.ac.uk
<https://eprints.whiterose.ac.uk/>

1 **Understanding the emplacement of Martian volcanic**
2 **rocks using petrofabrics of the nakhlite meteorites.**

3

4 **Luke Daly^{1,5,6*}, Sandra Piazzolo², Martin R. Lee¹, Sammy Griffin¹, Peter Chung¹,**
5 **Fabrizio Campanale¹, Benjamin E. Cohen¹, Lydia J. Hallis¹, Patrick W. Trimby³,**
6 **Raphael Baumgartner⁴, Lucy V. Forman⁵, Gretchen K. Benedix^{5,7}**

7 ¹School of Geographical and Earth Sciences, University of Glasgow, Glasgow, G12 8QQ,
8 UK.

9 ²School of Earth and Environment, University of Leeds, Leeds, LS2 9JT, UK

10 ³Oxford Instruments Nanoanalysis, High Wycombe, HP12 3SE, UK

11 ⁴School of Biological, Earth and Environmental Sciences, The University of New South
12 Wales, Kensington, NSW, 2052, Australia.

13 ⁵Space Science and Technology Centre, School of Earth and Planetary Sciences, Curtin
14 University, GPO Box U1987, Perth, WA 6845, Australia.

15 ⁶Australian Centre for Microscopy and Microanalysis, University of Sydney, Sydney 2006,
16 NSW, Australia.

17 ⁷Planetary Science Institute, 1700 East Fort Lowell, Suite 106 Tuscon, AZ, 85719-2395 USA

18 *luke.daly@glasgow.ac.uk

19

20 **Abstract**

21 In order to validate calculated ages of the Martian crust we require precise radiometric dates
22 from igneous rocks where their provenance on the Martian surface is known. Martian
23 meteorites have been dated precisely, but the launch sites are currently unknown. Inferring
24 the formation environment of a correlated suite of Martian meteorites can constrain the nature

25 and complexity of the volcanic system they formed from. The nakhlite meteorites are such a
26 suite of augite-rich rocks that sample the basaltic crust of Mars, and as such can provide
27 unique insights into its volcanic processes. Using electron backscatter diffraction we have
28 determined the shape-preferred and crystallographic-preferred orientation petrofabrics of four
29 nakhlites (Governador Valadares, Lafayette, Miller Range 03346 and Nakhla) in order to
30 understand the conditions under which their parent rocks formed. In all samples, there is a
31 clear link between the shape-preferred orientation (SPO) and crystallographic-preferred
32 orientation (CPO) of augite phenocrysts. This relationship reveals the three-dimensional
33 shape of the augite crystals using CPO as a proxy for SPO, and also enables a quantitative 3-
34 dimensional petrofabric analysis. All four nakhlites exhibit a foliation defined by the CPO of
35 the augite $\langle c \rangle$ axis in a plane, although individual meteorites show subtle textural variations.
36 Nakhla and Governador Valadares display a weak CPO lineation within their $\langle c \rangle$ axis
37 foliation that is interpreted to have developed in a combined pure shear/simple shear flow
38 regime, indicative of emplacement of their parent rock as a subaerial hyperbolic lava flow.
39 By contrast, the foliation dominated CPO petrofabrics of Lafayette and Miller Range 03346
40 suggest formation in a pure shear dominated regime with little influence of hyperbolic flow.
41 These CPO petrofabrics are indicative of crystal settling in the stagnant portion of cooling
42 magma bodies, or the flattening area of spreading lava flows. The CPO foliation of
43 Lafayette's is substantially weaker than Miller Range 03346, probably due to its higher
44 phenocryst density causing grain-grain interactions that hindered fabric development. The
45 CPO petrofabrics identified can also be used to determine the approximate plane of the
46 Martian surface and the line of magma flow to within $\sim 20^\circ$. Our results suggest that the
47 nakhlite launch crater sampled a complex volcanic edifice that was supplied by at least three
48 distinct magmatic systems limiting the possible locations these rocks could have originated
49 from on Mars.

50

51 **Keywords:** Mars, Martian meteorites, nakhlites, electron backscatter diffraction,
52 petrofabrics, magmatic petrogenesis.

53

54 **1. Introduction**

55 The petrogenetic study of Martian meteorites and their inferred geological environment can
56 help us constrain the specific site these rocks were launched from on the planet's surface.

57 Ultimately, this knowledge will provide ground truth for crater counting calculations of the
58 age of Mars' crust. In addition, the study of Martian igneous rocks provides insights into
59 volcanism on a planetary surface with stagnant lid tectonics. The nakhlite meteorites are a
60 suite of pyroxene-rich (predominantly augite; ~65-80 modal %) mafic igneous rocks from
61 Mars (Bogard & Johnson, 1983; Treiman, 2005; Corrigan et al., 2015). They are comprised
62 of elongate, subhedral to euhedral prisms of augite, rarer olivine phenocrysts, and varying
63 abundances of interstitial fine-grained mesostasis (Treiman, 2005). These meteorites also
64 contain minerals including phyllosilicates and carbonates that formed by post-magmatic
65 aqueous alteration (Ashworth & Hutchison, 1975; Bunch & Reid, 1975; Changela & Bridges,
66 2010; Hallis et al., 2012; Hicks et al., 2014; Bridges et al., 2019). The nakhlites have been
67 relatively mildly shocked (<15 GPa; Treiman, 2005) interpreted to be a result of impact-
68 ejection from the Martian surface in a single event (Treiman, 2005).

69

70 The petrogenesis of the nakhlites has conventionally been interpreted as either a single
71 intrusion or a thick lava flow (Harvey & McSween, 1992; Nyquist et al., 2001; Mikouchi et
72 al., 2003; Treiman, 2005; Day et al., 2006; Mikouchi et al., 2012; Richter et al., 2016). A
73 potential terrestrial analogue is Theo's flow (Ontario, Canada; Lentz et al., 1999). However,
74 their formation in a single magmatic event has recently been challenged by $^{40}\text{Ar}/^{39}\text{Ar}$

75 crystallization ages requiring at least four episodes of igneous activity within the nakhlite
76 meteorite suite over a timespan of ~91 Ma (i.e. 1416 ± 7 Ma to 1322 ± 10 Ma; Cohen et al.,
77 2017).

78
79 In this study we assess whether petrofabrics can be used to understand the conditions under
80 which the nakhlites formed, and so help to discriminate between the different models for their
81 emplacement (e.g. single vs multiple igneous bodies). Using hand specimen and transmitted
82 light petrography, shape-preferred orientations (SPOs) of elongate augite phenocrysts have
83 been reported for the meteorites Nakhla, Lafayette and Yamato (Y) 000593 (Bunch & Reid,
84 1975; Mikouchi et al., 2003). Berkley et al. (1980) described a foliation and lineation in
85 Governador Valadares, Nakhla and Lafayette, formed by the preferred orientation of the long
86 $\langle c \rangle$ axes of augite crystals. In contrast, recent studies that have used image processing to
87 describe crystal shapes and to determine the crystal size distributions have concluded that the
88 nakhlites lack a petrofabric (Lentz et al., 1999; Udry & Day, 2018). Lentz et al. (1999) also
89 concluded that the crystal size distribution of augite phenocrysts in nakhlites is characteristic
90 of steady state nucleation and continuous growth. However, these previous studies have been
91 limited by the difficulties inherent in relating 2D measurements of grain size and shape in
92 thin section to 3D shape and crystallographic orientations.

93
94 Different styles of emplacement of igneous rocks generate distinctive petrofabrics that can be
95 identified and quantified using 3D crystallographic information. For example, phenocryst-
96 bearing terrestrial lavas display a weak to moderately strong lineation in the long shape axis
97 of phenocrysts due to shear forces aligning long axes to the flow direction (Bhattacharyya,
98 1966). In some instances, a short shape axis lineation oriented perpendicular to the direction
99 of flow is also observed (Bascou et al., 2005; Boiron et al., 2013). Conversely, magmatic

100 fabrics derived from gravity settling in an intrusion or stagnant lava pond produce a short
101 shape axis lineation parallel to the gravitational force, as well as an associated, planar girdle
102 distribution in the long axis perpendicular to the gravitational force (e.g., Jackson, 1961;
103 George, 1978). Hence, crystal shape fabrics in terrestrial lavas have been used as kinematic
104 indicators to reconstruct their flow history (e.g., Shelley, 1985; Wada, 1992; Ventura et al.,
105 1996). In addition, numerical models predict that the development of a petrofabric is typically
106 dependent on the flow regime, where a combined lineation and foliation of the long shape
107 axes of crystals is predicted to form in a regime resulting from an oblate strain. Such strain
108 can occur in a so called “hyperbolic” flow characterized by a combination of simple and pure
109 shear flow (e.g. Merle, 1998; Iezzi & Ventura, 2002).

110
111 Unconstrained growth of a mineral grain in a fluid, such as molten rock, typically produces a
112 strong correlation between the shape of a crystal and its crystallographic orientation (e.g., the
113 crystal’s <c> axis being parallel to the long shape axis of the crystal; Benn & Allard, 1989).
114 These fabrics, such as 2D-SPO and crystallographic-preferred orientation (CPO), can be
115 quantitatively described through electron backscatter diffraction (EBSD) mapping (Prior et
116 al., 1999). Therefore, EBSD is a suitable tool for quantitatively investigating the petrofabrics
117 of the nakhlite meteorites and constraining the mechanisms of their magmatic emplacement.
118 Here we have used EBSD mapping to investigate the conditions under which Miller Range
119 (MIL) 03346, Lafayette, Governador Valadares and Nakhla formed. These meteorites are of
120 particular interest because they differ significantly in mineralogy, including the abundance of
121 olivine (Lafayette > Nakhla = Governador Valadares > MIL 03346) and mesostasis (MIL
122 03346 > Lafayette = Governador Valadares > Nakhla; Corrigan et al., 2015; Udry & Day,
123 2018), and also differ in the crystallinity of the mesostasis and thickness of reaction rims on
124 olivine and pyroxene (Treiman 2005; Mikouchi et al., 2003).

125

126 **2. Methods**

127 Thin sections of the nakhlite meteorites MIL 03346 (118), Lafayette (USNM 1505-5),
128 Governador Valadares (Natural History Museum, London) and Nakhla (WAM 12965) were
129 obtained on loan from museum collections. As such, they were not specifically cut relative to
130 the orientation of any fabrics in these meteorites such as lineations or foliations. These
131 sections were prepared for EBSD analysis by progressively mechanically polishing each
132 sample from 8 μm grit paper (five minutes) to 1 μm and 0.3 μm suspension of aluminium
133 balls in glycol (five minutes each). They were then polished further in a NaOH colloidal
134 silica (0.1 μm) suspension for four hours to remove the damaged layer from the initial
135 mechanical polish so as to provide a surface suitable for EBSD. Governador Valadares and
136 Nakhla were coated with 5 nm of carbon for high vacuum EBSD work at Macquarie
137 University, while MIL 03346 and Lafayette were not coated, in order to take advantage of the
138 variable pressure scanning electron microscope (VP-SEM) at the University of Glasgow.

139

140 SEM secondary electron imaging, as well as energy dispersive X-ray spectroscopy (EDS) and
141 EBSD data analysis of MIL 03346 and Lafayette used a Zeiss Sigma VP field emission gun
142 SEM (VP-FEGSEM) operated at a vacuum of 49 Pa, at the University of Glasgow. This
143 instrument is equipped with an Oxford Instruments X-Max 80 mm² silicon drift X-ray
144 detector and a NordlysMax² EBSD detector.

145

146 SEM, EDS and EBSD data were acquired for Nakhla and Governador Valadares using a Carl
147 Zeiss IVO SEM operated at high vacuum, at Macquarie University. This instrument is
148 equipped with a HKL NordlysNano high sensitivity EBSD detector.

149

150 In both SEM laboratories, EBSD data were acquired with and indexed using Oxford
151 Instruments' AZtec software. For all EBSD analyses, the samples were tilted to 70 °, the
152 standard angle used for EBSD, and data were collected at 20 kV/4-8 nA via the automated
153 Large Area Mapping module of AZtec 3.3. The rectangular areas analysed by EBSD were:
154 106.4 mm² at a step size of 4 µm for MIL 03346; 85.0 mm² at a step size of 4 µm for
155 Lafayette; 20.3 mm² at a step size of 15 µm for Governador Valadares; 13.3 mm² at a step
156 size of 15 µm for Nakhla. These analyses produced combined totals of 6.6 million, 5.3
157 million, 0.09 million and 0.06 million electron backscatter patterns (EBSP) for MIL 03346,
158 Lafayette, Governador Valadares, and Nakhla, respectively. The expected angular uncertainty
159 for each individual EBSD measurement is <0.5° (Borthwick and Piazzolo, 2010). In order to
160 facilitate rapid whole section mapping, EBSPs were analysed in Oxford Instruments AZtec
161 3.3 software using 4×4 binning, an exposure time of 30-40 ms, and a frame average of 1
162 frame. The mean angular deviation (MAD), which is an expression of the quality of pattern
163 indexing (<1 is considered appropriate), was 0.52-0.61 for augite in all samples. The data
164 were cleaned using Oxford Instruments HKL software Channel 5, involving a wildspike
165 correction to remove isolated data points, followed by an iterative 8-, and 7-point nearest
166 neighbour zero solution and a single 6-point nearest neighbour zero solution. This procedure
167 helps to define grains without creating artefacts (i.e. Bestmann & Prior, 2003; Watt et al.,
168 2006). As the thin sections being studied were prepared without reference to any rock fabric,
169 we define a reference frame where x = horizontal, y = vertical, and z = perpendicular (out of
170 the plane of the thin section), and which relates directly to the x, y, z orientation of the
171 rectangular analysis area chosen for EBSD maps. This reference frame is consistent for each
172 sample between maps, pole figures, and rose diagrams presented.

173

174 Grain boundaries within the datasets were defined by $<10^\circ$ misorientation across adjacent
175 pixels. To avoid grain statistical artefacts related to minute mesostasis grains and fractured
176 phenocrysts, only the grains larger than $100\ \mu\text{m}$ in circle equivalent diameter were used for
177 further analysis. We define a grain as an area that is fully enclosed by grain boundaries. Twin
178 boundaries in augite, which are defined by a 180° rotation around (100), (001), (204) or
179 (104), were disregarded so that twinned grains were not sampled multiple times.
180 Crystallographic and shape orientation data were extracted from a statistically significant
181 number of augite grains in each sample. More than 100 grains are required to define a
182 representative fabric in a given rock (e.g., Ismail & Mainprice, 1998; Watt et al., 2006) and
183 we analysed 1382 augite grains in MIL 03346, 2225 in Lafayette, 390 in Gobernador
184 Valadares, and 329 in Nakhla. To display any CPOs in the augite phenocryst population, one
185 representative crystallographic orientation was extracted per grain.

186
187 CPOs for the augite phenocrysts are assessed with reference to their three major
188 crystallographic axes ($\langle a \rangle = \langle 100 \rangle$, $\langle b \rangle = \langle 010 \rangle$, $\langle c \rangle = \langle 001 \rangle$). The poles to these axes are
189 plotted in a lower hemisphere, stereographic projection (pole figure), and the data are
190 contoured relative to the density of data points, expressed as multiples of uniform density
191 (m.u.d.).

192
193 In order to determine the strength of the CPO, two quantitative metrics were calculated: M-
194 index (Skemer et al., 2005) and J-index (Bunge, 2013). The M-index defines the variance in
195 uncorrelated misorientation angle distributions between the sample crystallographic data and
196 a theoretical random fabric by taking all major (low index) axes into account (e.g., for augite
197 $\langle 100 \rangle$, $\langle 101 \rangle$ and $\langle 001 \rangle$). An M-index of 0 represents a random crystallographic orientation
198 distribution while 1 denotes a single crystal. In contrast, the J-index (or texture index) is

199 defined as the volume-averaged integral of squared orientation density of a chosen axis (here
200 $\langle 001 \rangle$ was used). J-index values range from 1, representing a random crystallographic
201 orientation distribution, to infinity, which is a single crystal. For all nakhlites in this study,
202 the M-index and J-index were calculated using the MTEX toolbox for MATLAB with a
203 kernel halfwidth of 10 (Bachmann et al., 2010). Finally, we performed eigenvalue analysis to
204 quantify the dominant, crystallographic fabric type, distinguishing between point (P), girdle
205 (G), and random (R) fabric (Vollmer, 1990). This analysis (PGR) demonstrates whether a
206 specific axis forms a lineation (perfect alignment forming a “Point” fabric), a foliation
207 (alignment of grains in one plane forming a “Girdle” fabric), or none of the above (“Random”
208 fabric). For each major crystallographic axis, the contribution of P , G , or R can be calculated
209 from three normalized eigenvalues ($k_1 k_2 k_3$): $P = k_1 - k_3$, $G = 2(k_2 - k_3)$, and $R = 3k_3$.
210 The MATLAB-MTEX code for these calculations is provided in the supplementary materials.
211 Due to the nature of geological materials, pure 100% P or G endmembers are uncommon;
212 even rocks with strong foliations or lineations are unlikely to exhibit P or G values much
213 above 50%. Therefore, here we infer a random fabric only when $R > 90\%$. P or G values
214 between 10-30 % are interpreted as weak fabrics, while 30-50% denote moderate fabrics and
215 $>50\%$ represent a strong fabric.

216

217 **3. Results**

218 **3.1. Morphology of augite phenocrysts**

219 It is clear that grain boundaries are commonly formed by low index planes (i.e. facets) in the
220 EBSD data; hence grains represent phenocrysts. The augite phenocrysts are subhedral to
221 euhedral and exhibit an elongate shape parallel to their $\langle c \rangle$ crystal axis as evidenced in
222 crystals where the $\langle c \rangle$ axis is parallel to the plane of the thin section (Figure 1). The two
223 short shape axes correlate with the $\langle a \rangle$ and $\langle b \rangle$ crystal axes as evidenced in crystals where

224 the $\langle a \rangle$ and $\langle b \rangle$ crystal axes are parallel to the plane of the thin section. Thus, the augite
225 phenocrysts are prism-shaped, not tabular (Figure 1).

226

227 **3.2. SPO and CPO**

228 The long shape axes of augite phenocrysts in Nakhla and Governador Valadares lack a strong
229 2D-SPO, as evidenced by their rose diagrams lacking a distinct clustering of long shape axis
230 orientations (Figures 2B, 3B). By contrast, Lafayette and MIL 03346 have a clear 2D-SPO as
231 evidenced by the clustering of long shape axes in their rose diagrams (Figures 4, 5). Lafayette
232 is characterised by a relatively narrow spread of 2D-SPO ($\sim 40^\circ$), while MIL 03346 has a
233 wider spread ($\sim 80^\circ$) (Figures 4, 5).

234

235 CPO patterns differ between the four meteorites. Pole figure m.u.d. values for Nakhla, MIL
236 03346 and Governador Valadares highlight weak $\langle a \rangle$ crystal axis point maxima
237 perpendicular to a moderate $\langle c \rangle$ crystal axis girdle (Figures 2-4). Within the $\langle c \rangle$ crystal axis
238 girdle plane of Nakhla, MIL 03346 and Governador Valadares, clustering of higher m.u.d.
239 values in the pole figure reveals weak point maxima (Figures 2C, 3C, 5C). Lafayette pole
240 figure m.u.d. values show that its augite grains define a weak $\langle c \rangle$ crystal axis girdle (Figure
241 4C). There is a clear correlation between the 2D-SPO long axis and $\langle c \rangle$ axis CPO orientation
242 for MIL 03346 (Figure 5), which is consistent with our observations in Figure 1 that grain
243 shapes are crystallographically controlled (i.e., the $\langle c \rangle$ axis of augite correlates with long
244 crystal shape axis) and permits us to infer 3D-SPO information from the CPO data.

245

246 Quantitative textural metrics for the meteorites support the qualitative textural observations
247 from the contoured m.u.d. values in EBSD pole figures. The four naxhlites have J-indices of
248 2-3, which indicates a moderate $\langle c \rangle$ axis CPO (Figure 2-5). PGR metrics indicate that all

249 samples have a moderate girdle fabric in the $\langle c \rangle / (001)$ crystal axis (Figure 6), although this
250 fabric is weaker in Lafayette than in the other three nakhlites (Figure 6). In addition, Nakhla
251 and Gobernador Valadares exhibit a weak $\langle c \rangle$ crystal axis point fabric (Figure 6). This point
252 fabric is also apparent as high m.u.d. values contained within the girdle of the $\langle c \rangle$ crystal
253 axis pole figure (Figure 2C and 3C). With regards to the other crystallographic axes, there is a
254 weak (100) CPO point fabric in Nakhla, MIL 03346 and Gobernador Valadares. However, in
255 all four nakhlites the M-index is uniformly low (0.01-0.03) (Figure 2-5).

256

257 **4. Discussion**

258 We first appraise the potential of our sample set for describing petrofabrics in 3D, then
259 evaluate how the properties of magma can be inferred from the petrofabric of rocks that have
260 formed after its solidification. Based on this understanding we then discuss the magmatic
261 conditions under which the four nakhlites formed, and the implications of our findings for the
262 petrogenesis of the nakhlite suite as a whole.

263

264 **4.1. Inferring 3D fabrics from 2D data: limitations and implications**

265 For samples of modern terrestrial lava flows, their original orientation relative to the Earth's
266 surface, proximity to the original magmatic system, and flow direction are all known. This
267 crucial contextual information has been lost from the nakhlites as these meteorites were
268 impact ejected from Mars into space. In addition, at a hand specimen scale it is difficult to
269 unambiguously identify any fabrics, such as foliations or lineations. Therefore, the nakhlite
270 thin sections studied here, which are essentially 2D slices through these meteorites, would not
271 have been cut with respect to any visible rock fabrics so that any 2D-SPO identified may not
272 correspond to the maximum 3D-SPO. Thus, the absence of a 2D-SPO in the Nakhla and
273 Gobernador Valadares thin sections does not necessarily preclude its presence in these

274 meteorites. Fortunately, the shape of augite phenocrysts in the nakhlites is
275 crystallographically controlled, whereby the crystal c-axis is parallel to the long shape axis of
276 the crystal and the crystal b- and a- axes form the short shape axes (Figure 1). Thus, the
277 drawback of having a randomly selected 2D plane of observation inhibiting the
278 characterisation of a 3D-SPO can be overcome by using quantitative crystallographic
279 orientation of all axes derived from EBSD as a proxy for the full 3D-SPO of phenocrysts.
280 The following discussion therefore emphasises CPO rather than 2D-SPO, as the CPO is
281 independent of the cut of the thin section.

282

283 **4.2. The relationship between CPO fabrics and magmatic flow regimes**

284 Igneous rocks that contain phenocrysts with shape anisotropy (e.g., prismatic or tabular) in a
285 finely crystalline groundmass, usually exhibit distinct 3D-SPO and CPO fabrics that are
286 characteristic of specific magmatic regimes. These fabrics can be identified using EBSD
287 where crystal shape is crystallographically controlled (i.e., the long and short shape axes
288 correspond to crystallographic planes) (Figure 1). Three end-member fabrics can be
289 identified:

290

291 (1) Random crystallographic orientation. This fabric would lack clustering or distinct patterns
292 of crystal orientation (i.e., no preferred alignment of elongate phenocrysts). The absence of
293 CPO indicates a mode of emplacement whereby no consistent directional force has been
294 applied to the cooling phenocryst-matrix assemblage. Such magmatic environments include
295 both turbulent flow and flow characterized by instabilities, such as convection cells. Other
296 scenarios that would produce a random crystallographic orientation include: (i) a 2D simple
297 shear flow, where orientations fluctuate significantly and can cyclically reach minimum
298 values; (ii) high phenocrysts to matrix ratios that inhibit phenocryst rotation and so fabric

299 development (Ježek et al., 1996). This fabric is not observed in any of the nakhlites studied
300 here.

301

302 (2) A CPO that is characterised by one or two crystal axes lying in a plane is called a
303 magmatic foliation (Paterson et al., 1998). Pole figures with such a CPO show a girdle
304 distribution of the long axis of prism shaped phenocrysts, and two girdles of the two longest
305 axes of tabular phenocrysts. This type of CPO indicates a deformation regime dominated by
306 pure shear or flattening flow with $\sigma_1 > \sigma_2 = \sigma_3$. Such a pure shear regime occurs during
307 gravitational crystal settling and compaction in quiescent areas of stagnant magmatic bodies,
308 such as lava pools and ponds, or magmatic intrusions (Merle, 1998; Iezzi & Ventura, 2002).
309 All nakhlites exhibit this fabric, but it is dominant in Lafayette and MIL 03346 (Figure 2, 3,
310 4, 5).

311

312 (3) A CPO featuring a distinct alignment of the long axes of tabular or prismatic crystals and
313 a random orientation of the other crystallographic axes produces a lineation petrofabric. In a
314 pole figure, this CPO is usually expressed by point maxima for the long axis and a
315 circular/girdle distribution of the other axes. Such a fabric develops in dominantly
316 constrictional flows whereby $\sigma_1 = \sigma_2 \gg \sigma_3$. Such a CPO is expected to be generated locally in
317 transpressional flow (Fossen & Tikoff, 1998; Tikoff & Fossen, 1999), where flow is
318 partitioned into constrictional and simple shear flow. Another scenario would be a plug flow
319 (Johnson, 1970), as occurs in lava tubes (Peterson et al., 1994). This fabric is not observed in
320 any of the nakhlites studied here.

321

322 Many natural examples have mixtures of these end-member CPOs. Most importantly, within
323 any flow that has both a flattening, pure shear component and a directional, simple shear

324 component, a foliation is often produced alongside a lineation (Merle, 1998; Iezzi & Ventura,
325 2002). In a subaerial magmatic flow, both rotational (simple shear) and non-rotational,
326 flattening (pure shear) are likely to occur, where the simple shear component dominates close
327 to the shear plane (e.g., Merle, 1998 Figure 8; Iezzi & Ventura, 2002). This shear plane, in
328 the case of a subaerial lava flow, is situated at the base of the flow in contact with the
329 bedrock. The magnitude of the pure shear component depends on the effect of overburden
330 causing compaction, as well as on the timescales of melt/mesostasis cooling and
331 crystallisation. Flow dominated by simple shear favours a more pronounced point
332 maxima/lineation, whereas flow dominated by pure shear favours girdle distribution/foliation.
333 In a divergent flow (i.e., flowing lava that spreads out), the volume of flow with a significant
334 flattening component is relatively large and close to the bedrock, whereas constrictional flow
335 is dominant close to the top of the lava. Such a flow mixture is consistent with the
336 petrofabrics observed in Governador Valadares and Nakhla (Figure 2, 3).

337
338 In magmatic systems that contain both phenocrysts and matrix (i.e., melt, mesostasis), the
339 volume ratio of these two components further influences the strength of a CPO. At low ratios
340 (i.e., large amounts of matrix and few phenocrysts), the strength will oscillate, but may
341 temporarily be high (Jezek et al., 1996; Piazzolo et al., 2002), whereas at high
342 phenocryst/matrix ratios (e.g. where >40% of phenocrysts interact with each other) the CPO
343 strength is more stable but usually less pronounced (Ildefonse et al., 1992). Therefore, in
344 phenocryst-rich lavas such as some of the nakhlites interactions between adjacent
345 phenocrysts can inhibit rotation and so hinder fabric development. This process may cause
346 substantial variations in fabric strength between and within nakhlites, or even produce some
347 regions on the hand specimen to outcrop scale that completely lack a fabric (Ildefonse et al.,
348 1992; Iezzi & Ventura, 2002).

349

350 **4.3. Magmatic environments for the four nakhlites**

351 All four nakhlites have petrofabrics (i.e. non-random 3D-SPOs and CPOs). This indicates
352 that their parent magmas were subject to non-chaotic flow and so cannot have cooled in a
353 turbulent regime.

354

355 The 2D-SPO data suggest that the petrofabrics of Nakhla and Governador Valadares (no
356 apparent 2D-SPO, Figures 2B, 3B) are different to MIL 03346 and Lafayette (strong 2D-
357 SPO; Figures 4B, 5B). However, due the arbitrary orientations of the thin sections, 2D-SPO
358 cannot be solely used to reliably distinguish nakhlite fabrics and petrographic relationships.

359 EBSD pole figures, PGR plots and J-index metrics indicate that all of the nakhlites have a
360 weak to moderate girdle maxima defined by the alignment of the long $\langle c \rangle$ crystal axes of
361 augite phenocrysts within a plane, which represents a magmatic foliation (Figures 2-6).

362 Additionally, EBSD crystal pole figures and PGR plots separate the nakhlites into two sets:

363 Nakhla + Governador Valadares, and Lafayette + MIL 03346. Nakhla and Governador

364 Valadares have a weak but clear $\langle c \rangle$ crystal axis lineation, contained within the $\langle c \rangle$ crystal
365 axis foliation (Figures 2C, 3C, 6). The EBSD pole figure for MIL 03346 is suggestive of a

366 $\langle c \rangle$ crystal axis lineation contained within the $\langle c \rangle$ crystal axis foliation (Figure 4), although

367 such a fabric is not revealed by the PGR ternary diagram (Figure 6). By contrast, both the

368 EBSD pole figures and PGR data of Lafayette show only a crystal foliation. Therefore, the

369 presence of a $\langle c \rangle$ crystal axis lineation petrofabric distinguishes Nakhla and Governador

370 Valadares from MIL 03346 and Lafayette, in that Nakhla and Governador Valadares show a

371 $\langle c \rangle$ crystal axis lineation. This said, the PGR values of all three crystallographic axes of

372 Lafayette show that its crystal foliation is much weaker than the other three nakhlites, as

373 evidenced by a lower G value in the PGR plot (Figure 6). Thus, the four samples should be
374 divided into three sets from their CPO petrofabrics.

375

376 The M-index results suggest that all samples have a random fabric, which contradicts the
377 other quantitative petrographic metrics described above. This apparent discrepancy can be
378 readily explained because the M-index gives equal weighting to the three major
379 crystallographic axes. Thus, the augite crystals will have a low M-index because their $\langle c \rangle$
380 axis is aligned to form a weak to moderate girdle fabric whereas the $\langle a \rangle$ and $\langle b \rangle$ axes are not
381 (Figure 6); the M-index value for the whole rock is therefore much lower than expected from
382 the observed $\langle c \rangle$ crystal axis fabric. Based on all other data (i.e., J-index, pole figure, PGR),
383 we conclude that these nakhlites contain at least a $\langle c \rangle$ crystal axis girdle maxima and that
384 Nakhla and Gobernador Valadares are likely to be distinct from MIL 03346, and are certainly
385 different to Lafayette.

386

387 The common crystallographic petrofabrics of Nakhla and Gobernador Valadares (Figures 2,
388 3) mirror other petrologic similarities. These two meteorites have a near identical modal
389 mineralogy, a similar major and minor element geochemistry, and comparable cooling rates
390 as inferred from the thickness of Fe-rich rims in olivine and the width of plagioclase laths
391 (Treiman, 2005; Corrigan et al., 2015; Udry & Day, 2018 and references therein). These
392 similarities therefore suggest that the two rocks cooled and crystallised in a comparable
393 regime and from a compositionally similar melt and therefore, these two nakhlites may
394 sample the same lava flow. This hypothesis could be tested by high-resolution $^{40}\text{Ar}/^{39}\text{Ar}$
395 geochronology as used by Cohen et al. (2017) to corroborate the quantitative textural and
396 geochemical analyses of these meteorites that suggest Nakhla and Gobernador Valadares
397 formed in the same flow (Udry and Day 2018). Our finding of a weak-moderate

398 crystallographic foliation and lineation in Nakhla and Governador Valadares is consistent
399 with pure shear, with a small but distinct component of simple shear. Such forces are
400 suggestive of a hyperbolic flow regime as observed mainly in subaerial lava flows on Earth
401 (Merle, 1998; Iezzi & Ventura, 2002).

402
403 MIL 03346 and Lafayette have little or no crystallographic lineation, and display moderate
404 and weak <c> crystal axis foliations, respectively. These crystallographic petrofabrics and
405 inferred 3D-SPO's imply a regime strongly dominated by pure shear with gravitational
406 settling of crystals, such as a lava lake, sill or stagnant regime of a lava flow. One could also
407 envisage a spreading lava flow, where a pure shear/constrictional stress regime dominated.
408 Differences between these two meteorites in the strength of their <c> crystal axis foliation
409 and inferred 3D-SPO, indicates that they were emplaced under contrasting conditions,
410 although the higher phenocryst to matrix ratio of Lafayette relative to MIL 03346 may have
411 also contributed to its weaker CPO fabric strength. This conclusion is consistent with their
412 $^{40}\text{Ar}/^{39}\text{Ar}$ ages, which differ by ~70 Ma (Cohen et al., 2017), and previous geochemical and
413 textural analysis of these rocks (Udry and Day 2018) which suggest that they formed in
414 discrete magmatic events.

415

416 **4.4. Relative positions within each individual magma body**

417 The chemical zoning in nakhlite olivine shows that out of the four meteorites studied here,
418 MIL 03346 cooled relatively rapidly, whereas Lafayette cooled much more slowly (Treiman,
419 2005; Day et al., 2006; Mikouchi et al., 2012). Cooling rate can be used as a proxy for former
420 position of the meteorite within its parent magmatic body (i.e., MIL 03346 was from close to
421 the top of its magmatic unit and Lafayette crystallised at a greater depth within its magmatic
422 unit where heat loss was slower; Treiman, 2005; Day et al., 2006; Mikouchi et al., 2012).

423 Petrofabric results are also consistent with such relative positions within their discrete magma
424 bodies. Specifically, the weaker CPO and lower proportion of mesostasis of Lafayette relative
425 to MIL 03346 implies that Lafayette cooled at the base of a relatively thick magma body,
426 where the compaction of crystals during settling expelled melt, and the resulting high
427 abundance of phenocrysts inhibited CPO and 3D-SPO fabric development (Ildefonse et al.,
428 1992; Iezzi & Ventura, 2002). These conclusions are also consistent with the equilibrated
429 composition of the olivine and pyroxene phenocrysts and crystalline nature of the mesostasis
430 described previously (Day et al., 2006). The greater CPO strength of MIL 03346 (Figure 6)
431 and its high abundance of mesostasis (Day et al., 2006) suggests that it crystallised rapidly in
432 the upper part of a thick lava flow, or alternatively the lower part of a flattening thin flow.
433 Under these conditions the expulsion of mesostasis due to crystal compaction would have
434 been minimised so that 3D-SPO fabric development (inferred from CPO) would not be
435 inhibited. This scenario is again consistent with previous models (Day et al., 2006) based on
436 the meteorite's disequilibrium mineral textures, such as rimmed olivine and pyroxene, and
437 evidence for rapid cooling from the fine grained-glassy mesostasis.

438
439 Lafayette and MIL 03346 must sample distinct magmatic units as they are temporally
440 separated by ~70 Ma (Cohen et al., 2017), while their petrofabrics are consistent with a
441 similar emplacement mechanism within cumulate flows (Lentz et al., 1999; Mikouchi et al.,
442 2003; Treiman, 2005; Day et al., 2006; Mikouchi et al., 2012; Udry & Day, 2018). Thus, the
443 volcanic system that generated the nakhlites had several episodes of similar volcanic activity
444 producing similar igneous units over at least 70 Ma.

445
446 Nakhla and MIL 03346 are temporally indistinguishable (Cohen et al., 2017) despite having a
447 distinct CPO petrofabric (Figure 6, Treiman, 2005; Day et al., 2006; Hallis et al., 2012;

448 Corrigan et al., 2015; Udry & Day, 2018). There are two ways to reconcile this apparent
449 contradiction. One is that they formed in two different magmatic environments and events,
450 which cannot be resolved by $^{40}\text{Ar}/^{39}\text{Ar}$ geochronology. Alternatively, if Nakhla and MIL
451 03346 were contemporaneous their different petrofabrics could be explained by their parent
452 lava being internally complex, for example exhibiting both hyperbolic flow and gravity
453 settling (e.g. a lava flow feeding into a lava lake). Such internal heterogeneity could have
454 been developed over length scales of less than 3 km (i.e., as constrained by the size of the
455 crater formed during the nakhlite impact-ejection event, Fritz et al., 2005). Similar textural
456 heterogeneity has been described in terrestrial lava flows such as Theo's flow (Lentz et al.,
457 1999) as well as sills and dykes (Shelley, 1985; Wada, 1992). Locally these 3D-SPO fabrics
458 inferred from CPO may be stronger or weaker through grain-grain interactions during flow
459 that result in episodic weakening and/or strengthening of the fabric (Ildefonse et al., 1992;
460 Iezzi & Ventura, 2002; Jezek et al., 1996; Piazzolo et al., 2002) consistent with the higher
461 mesostasis/phenocryst ratio of MIL 03346 relative to Nakhla (Treiman, 2005; Day et al.,
462 2006; Corrigan et al., 2015; Udry & Day, 2018). For these specific meteorites, the higher
463 mesostasis abundance of MIL 03346 has been suggested to form as a quench cooled break
464 out from the front of a lava flow (Hallis et al., 2012). Such a rapid unidirectional forcing
465 might generate the gravity settling CPO texture we observe in MIL 03346 (Figures 4, 6).
466 Nakhla cooled over a longer time period, evidenced by the equilibrated textures of the
467 phenocrysts (Treiman, 2005), and so likely formed within the main portion of the flow, and
468 therefore had time to generate the hyperbolic flow CPO fabric (Figures 2, 6). The scenario
469 above is however, but one solution of many that can occur in complex volcanic systems.

470

471 The presence or absence of crystallographic lineations and/or foliations, coupled with
472 equivalent 3D-SPO development (inferred from the CPO data), can be used to identify the

473 relative orientations of the Martian surface and the approximate line of flow of the parent
474 magmas of these meteorites. Provided that the 3D shape orientation of augite phenocrysts in
475 the nakhlites is an expression of a gravity driven processes, the 3D-SPO/CPO foliation plane
476 would be sub-parallel to the Martian surface. As the four nakhlites all exhibit a <c> crystal
477 axis foliation, the trace of this girdle is within 10-20° the plane of surface of Mars (the red
478 dashed line in Figures 2C, 3C, 4C, and 5C).

479
480 In the presence of a significant simple shear component, any 3D-SPO lineation (inferred from
481 the CPO) generated would define the line along which the parent lava flowed. Nakhla and
482 Gobernador Valadares exhibit such a lineation in their <c> crystal axes and as such
483 represents the line of magmatic flow in these rocks (the white dashed circle in the <c> axis in
484 Figure 2C and 3C). However, care must be taken when interpreting flow lines from 3D-
485 SPO/CPO lineations, as models suggest that such lineations form at a slight angle (<20°) to
486 the flow direction (Passchier, 1982). Using these crystallographic petrofabrics to produce
487 new thin sections that are parallel and perpendicular to these fabrics would enable
488 identification of other way up criteria and the direction of the gravitational force or direction
489 of flow, and as such the meteorites' position relative to the Martian surface.

490

491 **4.5. Geological settings for the origin of the nakhlites.**

492 The nakhlite meteorites are, in a broad sense, petrographically similar (Treiman, 2005) as
493 they have the same general composition and general matrix-phenocryst characteristics.
494 However, there are distinct petrographic differences between them and within individual
495 meteorites, such as mesostasis abundance, phenocryst size, and reaction rim thickness
496 representing different phenocryst equilibrium (e.g., Mikouchi et al., 2003; Corrigan et al.,
497 2015; Udry & Day, 2018). Furthermore, previous reports of the presence or absence of 2D-

498 SPO fabrics within the nakhlite meteorites are contradictory. Some studies have described
499 foliations and even lineations (Bunch & Reid, 1975; Berkley et al., 1980; Mikouchi et al.,
500 2003), while others report no distinct fabric, maybe because they used image analysis that
501 cannot extract CPO information (Lentz et al., 1999; Udry & Day, 2018). Our results
502 demonstrate that the nakhlites do preserve 3D-SPO petrofabrics inferred from CPO, and the
503 strength and type of fabrics observed varies between meteorites owing to contrasting
504 emplacement mechanisms. In turn, these findings support the suggestion that the nakhlites are
505 from different magmatic units (Cohen et al., 2017).

506

507 There is an ongoing debate regarding the emplacement environment of these rocks relative to
508 the Martian surface. Both subaerial flows and subsurface sills have been suggested (Treiman,
509 2005) but it is unclear how these environments could be distinguished. For example, cooling
510 rate could be used, but it is also a function of the thickness of a lava flow/intrusion, and in the
511 case of an intrusion, the depth of emplacement is also a factor. Even the petrofabrics
512 indicative of flow described in this study, while more likely to have formed within a subaerial
513 lava flow, are not a unique signature; similar petrofabrics have been reported in parts of
514 terrestrial sills and dykes (Shelley, 1985; Wada, 1992). The fact that the nakhlites have been
515 ejected from Mars in an impact can also be used to constrain emplacement environment.
516 Rocks will be excavated from depths of up to 1/5 of the impactor diameter (Artemieva &
517 Ivanov, 2004) so that a bolide producing a 10 km crater would eject rocks from a maximum
518 depth of ~65 m (Cohen et al., 2017). These shallow levels would favor lava flows as
519 intrusions would be more abundant at depth beneath the volcanic edifice (assuming low rates
520 of erosion). The nakhlite's mild shock metamorphism also favors shallow ejection depths
521 (Artemieva & Ivanov, 2004; Fritz et al., 2005; Treiman, 2005), although again this is not a
522 unique requirement. Conversely, the phenocryst/mesostasis ratio of the nakhlites is generally

523 above the point of critical crystallinity (~55%) that would inhibit eruption and flow of these
524 magmas and would indicate emplacement as a sill rather than a lava flow. However, our CPO
525 data indicate that some mesostasis may have been lost through compaction of phenocrysts
526 during simple and pure shear – an observation which may indicate that these lavas were once
527 more mesostasis-rich. This would imply that sub-aerial emplacement remains plausible.

528

529 The variety of petrofabrics present in the nakhlite meteorites suggest a diverse range of
530 magmatic emplacement mechanisms and lava thickness at the nakhlite source
531 volcano/volcanoes. Governador Valadares and Nakhla display both pure/flattening and
532 simple shear flow components consistent with subaerial flow, while MIL 03346 and
533 Lafayette likely formed at the top and bottom, respectively, of a highly pure shear/flattening
534 dominated regime consistent with stagnant lava lake. The emplacement mechanisms inferred
535 for these meteorites would mean that these fabrics would be transient (rapidly being created
536 and destroyed over a cm-m scale). Therefore, some regions within a given nakhlite meteorite
537 may have no distinct crystallographic fabric, which may explain the apparent absence of 2D-
538 SPO petrofabrics found in previous nakhlite studies (e.g., Udry & Day, 2018). This
539 possibility, means care must be taken when extrapolating petrofabrics observed in one thin
540 section as representative of the whole rock and inferring formation environment. However,
541 this could readily be tested by EBSD analysis of the samples used in previous studies and
542 ideally expanded to include several sections from different portions of each meteorite and/or
543 paired stones.

544

545 All cosmogenic exposure measurements undertaken on the nakhlites indicate that these rocks
546 were ejected from the Martian surface in a single impact event at 11 Ma (Benn & Allard,
547 1989; Nyquist et al., 2001; Treiman, 2005; Cohen et al., 2017). The diversity of petrofabrics

548 observed here and reported elsewhere implies that the impact site is at an edifice with
549 prolonged subaerial magmatic activity including lava flows of variable thickness, as well as
550 loci of gravitation crystal settling and melt expulsion. Such a complex volcanic setting
551 exhibited by the nakhlite petrofabrics may potentially rule out ‘simpler’ geological terrains on
552 Mars as candidates for the Nakhlite launch site.

553

554 **5. Conclusions**

555 Identifying the launch site for the nakhlite meteorites is critical for calibrating the age of the
556 Martian surface. Through petrographic analysis we can understanding how these nakhlite
557 meteorites were emplaced to constrain the geological setting and terrain in which they
558 formed. Thus, providing tighter constraints on the possible terrains sampled by the Nakhlite
559 source crater. In this study, large area EBSD mapping of four Martian igneous rocks has
560 revealed a diversity of 3D-SPO petrofabrics inferred from CPO data that indicate cooling and
561 crystallisation in two distinct magmatic environments.

562

- 563 1) Nakhla and Governador Valadares. These meteorites have similar foliation and
564 lineation petrofabrics consistent with emplacement in a magmatic flow – either a lava
565 flow, or a sill that was undergoing magma flow.
- 566 2) MIL 03346 and Lafayette exhibit only a foliation consistent with crystal settling in
567 either a quiescent magmatic system or the flattening regime in the lower parts of a
568 spreading lava flow. The substantially lower fabric strength in Lafayette is likely due
569 to phenocryst abundance inhibiting fabric development. The distinct crystallisation
570 ages of these two meteorites indicate that at least two spreading lava flows were
571 generated from the same region of the Martian crust over 70 Ma.

572

573 These petrofabrics constrain both the line of flow and the plane of the Martian surface. The
574 two distinct modes of emplacement imply a complex magmatic system in the vicinity of the
575 nakhlite ejection site. We propose that the crater formed during impact ejection of the
576 nakhlites is superimposed upon a complex volcanic edifice. Thus, any ~11 Ma crater
577 candidates for the nakhlite source must fulfil this criterion and craters superimposed on
578 relatively simple volcanic terrains are relatively poor candidates for the nakhlites. These new
579 petrographic constraints can aid in focusing the search for the elusive nakhlite source crater.
580 The approach outlined here can also be applied to understand other volcanic systems on Mars
581 and terrestrial planets in the solar system.

582

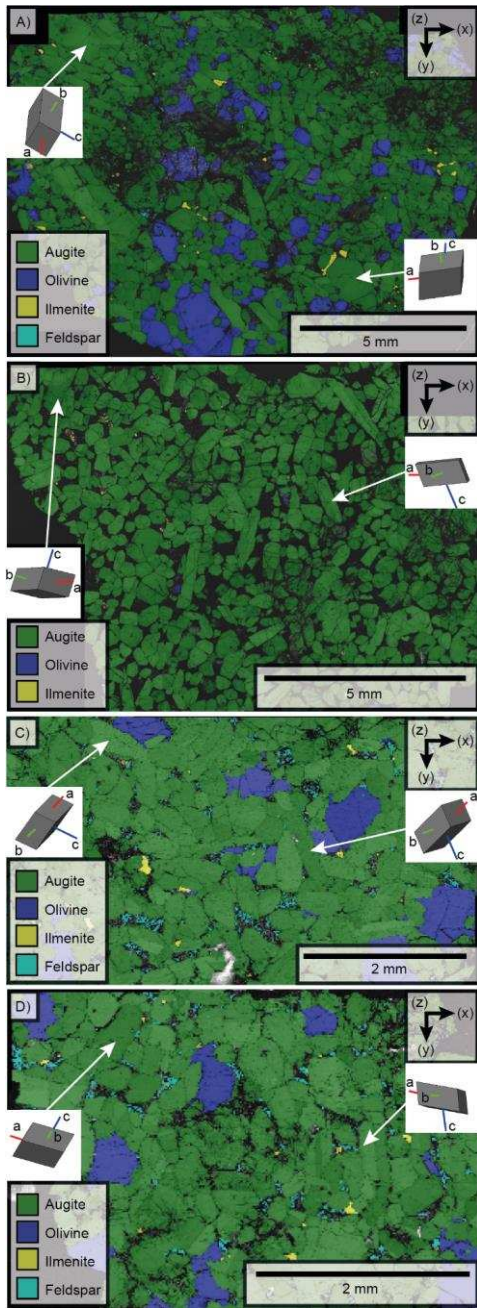
583 **6. Acknowledgements**

584 We thank the following institutions for providing the meteorite samples: Smithsonian
585 Institute, NASA Meteorite Working Group, Natural History Museum London (loan of
586 Governador Valadares), Macovich Collection, The Western Australia Museum, and the
587 Japanese Antarctic Meteorite Research Centre. US Antarctic meteorite samples are
588 recovered by the Antarctic Search for Meteorites (ANSMET) program which has been
589 funded by NSF and NASA, and characterised by the Department of Mineral Sciences of the
590 Smithsonian Institution and Astromaterials Acquisition and Curation Office at NASA
591 Johnson Space Centre. This work was funded by the Science and Technology Facilities
592 Council through grants ST/N000846/1 and ST/H002960/1 to M.R.L). The authors
593 acknowledge the facilities, and the scientific and technical assistance, of the Australian
594 Microscopy & Microanalysis Research Facility at the Centre for Microscopy,
595 Characterisation and Analysis, University of Western Australia and the Imaging
596 Spectroscopy and Analysis Centre, University of Glasgow. The authors would also like to

597 thank Prof. Arya Udry, one anonymous reviewer and handling editor Prof. Tamsin Mather for
598 their invaluable comments and suggestions to improve this manuscript.

599

600 **Figure Captions**

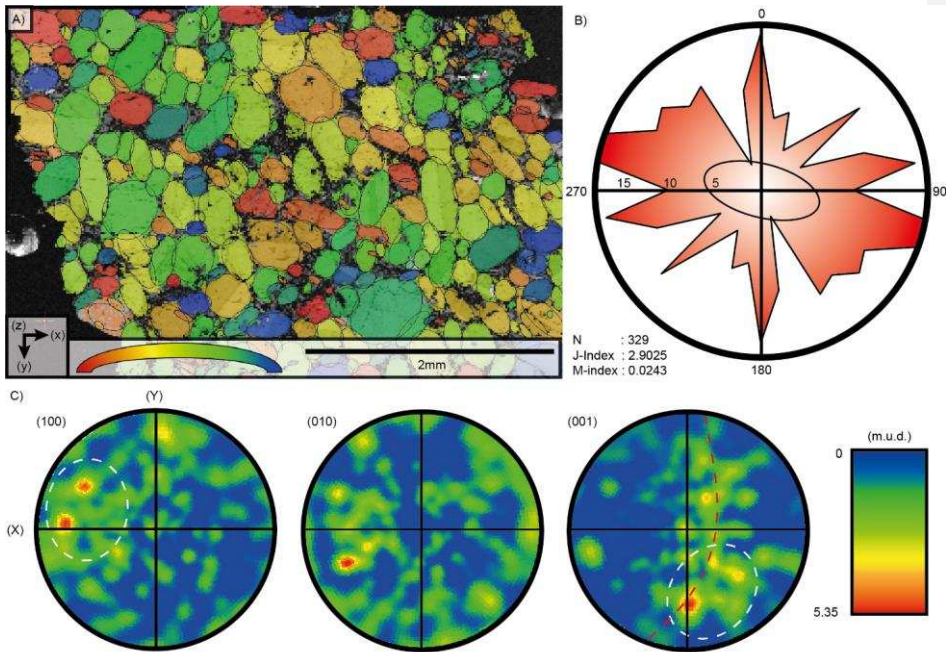


601

602 Figure 1

603 EBSD maps of Lafayette (A), MIL 03346 (B), Governador Valadares (C), and Nakhla (D),
604 highlighting different mineral phases by discrete colours (see key). The insets are 3D
605 visualisations of selected crystals, which reveal that crystal shapes correlate with
606 crystallographic orientations whereby the long shape axis corresponds to the $\langle c \rangle$ crystal axis
607 and the short shape axes to the crystallographic $\langle a \rangle$ and $\langle b \rangle$ crystal axes. In addition, it is
608 clear that grain boundaries are commonly formed by low index planes (i.e., facets); hence
609 grains represent phenocrysts.
610

611

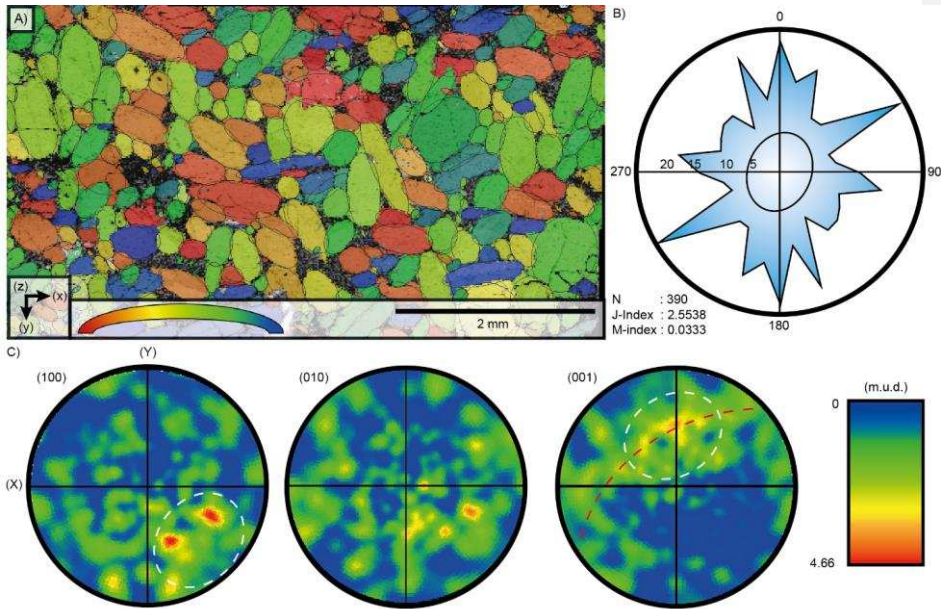


612

613 Figure 2

614 Quantitative EBSD characterisation of Nakhla. A) EBSD map, colour coded using the 2D-
615 SPOs of augite crystals. B) Rose diagram of long axis 2D-SPOs. C) Contoured pole figures
616 of the main crystallographic axes $\langle a \rangle$, $\langle b \rangle$ and $\langle c \rangle$. The red dashed line represents the 3D-
617 SPO foliation plane inferred from the CPO, and the plane of the Martian surface, whereas the
618 white dashed lines represent point maxima; in the $\langle c \rangle$ crystal axis the point maxima
619 represent the line of magmatic flow. M and J index values are listed with the pole figures: N
620 denotes the number of grains measured: m.u.d. = multiples of uniform density.

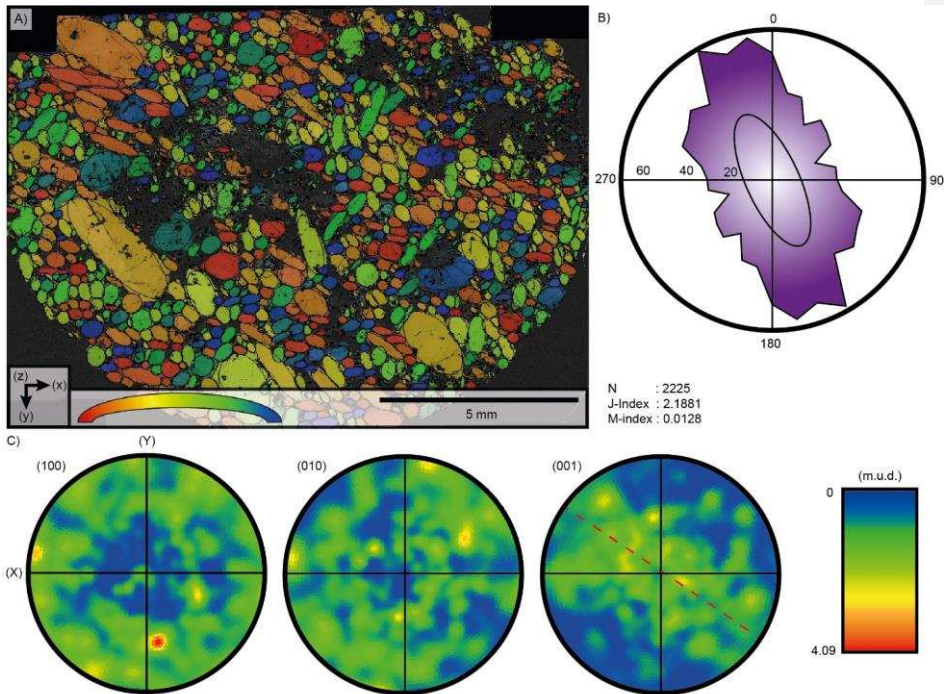
621



622

623 Figure 3

624 Quantitative EBSD characterisation of Gobernador Valadares. A) EBSD map, colour coded
 625 using the 2D-SPOs of augite crystals. B) Rose diagram of long axis 2D-SPOs. C) Contoured
 626 pole figures of the main crystallographic axes $\langle a \rangle$, $\langle b \rangle$ and $\langle c \rangle$. The red dashed line
 627 represents the 3D-SPO foliation plane inferred from the CPO, and the plane of the Martian
 628 surface, whereas the white dashed lines represent point maxima; in the $\langle c \rangle$ crystal axis the
 629 point maxima represents the line of magmatic flow. M and J index values are listed with the
 630 pole figure: N denotes the number of grains measured: m.u.d. = multiples of uniform density.

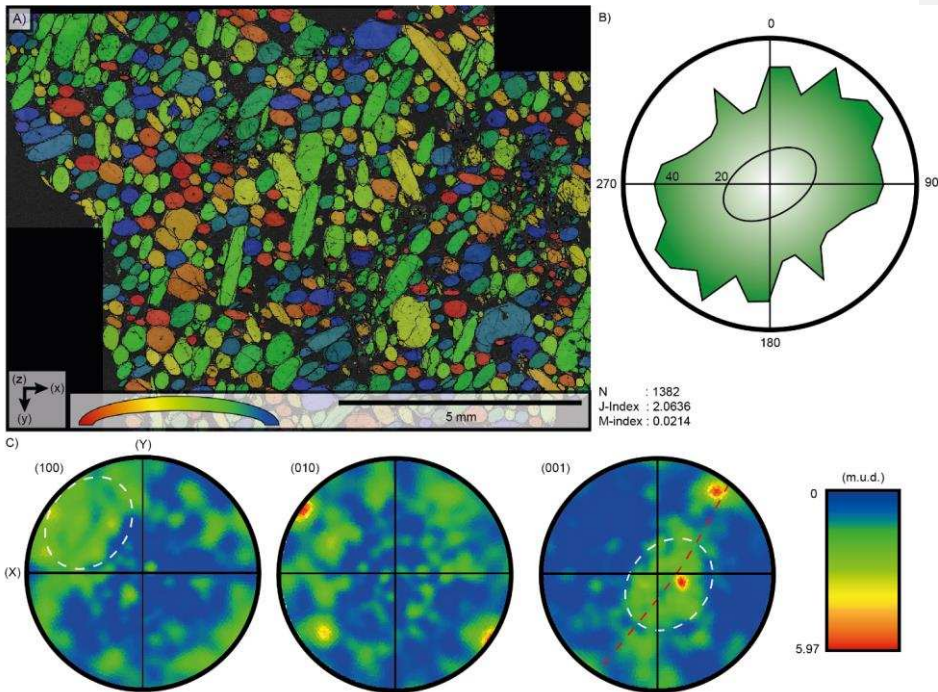


631

632 Figure 4

633 Quantitative EBSD characterisation of Lafayette. A) EBSD map, colour coded using the 2D-
 634 SPOs of augite crystals. B) Rose diagram of long axis 2D-SPOs. C) Contoured pole figures
 635 of the main crystallographic axes $\langle a \rangle$, $\langle b \rangle$ and $\langle c \rangle$. The red dashed line represents the 3D-
 636 SPO foliation plane inferred from the CPO data, and the plane of the Martian surface. M and
 637 J index values are provided with the pole figure: N denotes the number of grains measured:
 638 m.u.d. = multiples of uniform density.

639

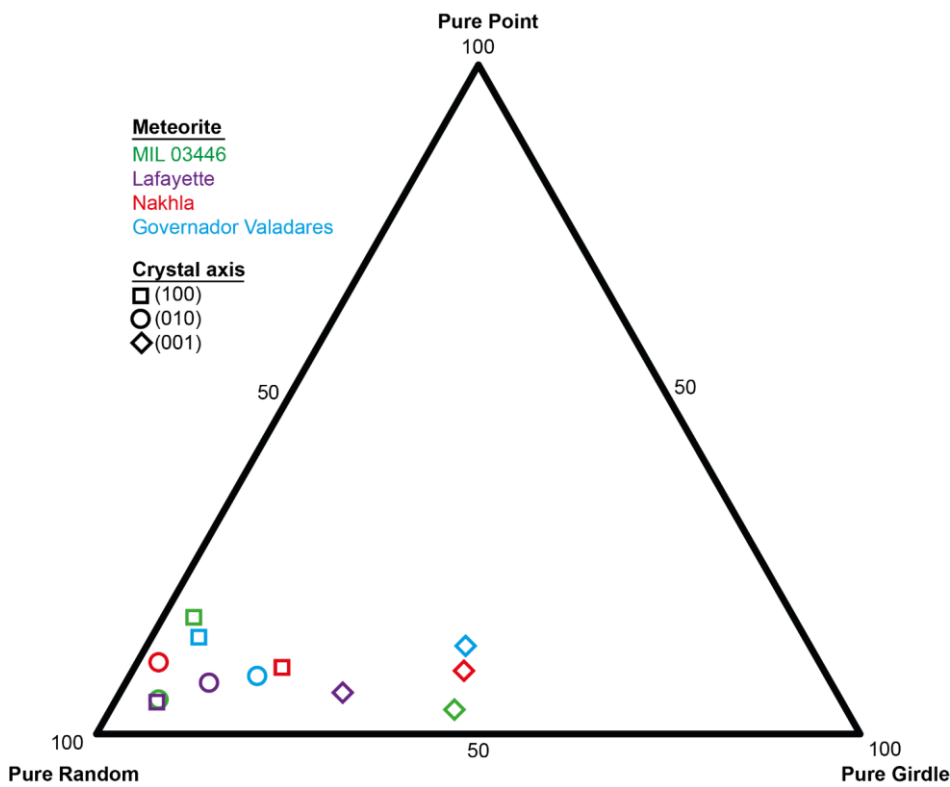


640

641 Figure 5

642 Quantitative EBSD characterisation of MIL 03346. A) EBSD map, colour coded using the
 643 2D-SPOs of augite crystals. B) Rose diagram of long axis 2D-SPOs. C) Contoured pole
 644 figures of the main crystallographic axes $\langle a \rangle$, $\langle b \rangle$ and $\langle c \rangle$. The red dashed line represents
 645 the 3D-SPO foliation plane inferred from the CPO data, and the plane of the Martian surface,
 646 whereas the white dashed lines represent point maxima; in the $\langle c \rangle$ crystal axis the point
 647 maxima represents the line of magmatic flow. M and J index values are provided with the
 648 pole figure: N denotes the number of grains measured: m.u.d. = multiples of uniform density.

649



650 Pure Random 50 50 100 Pure Girdle

651 Figure 6

652 Ternary diagram of the dominant 3D-SPO crystal fabrics inferred from the CPO data (pure
 653 random, pure girdle, pure point maxima) in Nakhla, Gobernador Valadares, Lafayette, and
 654 MIL 03346. We infer a random fabric for $R > 90\%$. P or G values between 10-30% are
 655 interpreted as weak fabrics, 30-50% as moderate fabrics and $>50\%$ as a strong fabric. There
 656 is a moderate to strong girdle in the (001) of all meteorites, and a weak point in the (001) of
 657 Gobernador Valadares and Nakhla and the (100) axis of all studied nakhlites except
 658 Lafayette.

659

660

661 **REFERENCES CITED**

- 662 Artemieva, N., & Ivanov, B. (2004). Launch of Martian meteorites in oblique impacts.
663 *Icarus*, 171(1), 84-101.
- 664 Ashworth, J., & Hutchison, R. (1975). Water in non-carbonaceous stony meteorites. *Nature*,
665 256(5520), 714-715.
- 666 Bachmann, F., Hielscher, R., Jupp, P. E., Pantleon, W., Schaeben, H., & Wegert, E. (2010).
667 Inferential statistics of electron backscatter diffraction data from within individual
668 crystalline grains. *Journal of Applied Crystallography*, 43(6), 1338-1355.
- 669 Bascou, J., Camps, P., & Dautria, J. M. (2005). Magnetic versus crystallographic fabrics in a
670 basaltic lava flow. *Journal of Volcanology and Geothermal Research*, 145(1-2), 119-
671 135.
- 672 Benn, K., & Allard, B. (1989). Preferred mineral orientations related to magmatic flow in
673 ophiolite layered gabbros. *Journal of Petrology*, 30(4), 925-946.
- 674 Berkley, J., Keil, K., & Prinz, M. (1980). Comparative petrology and origin of Governador
675 Valadares and other nakhlites. 11th Lunar and Planetary Science Conference, 1089-
676 1102.
- 677 Bestmann, M., & Prior, D. J. (2003). Intragranular dynamic recrystallization in naturally
678 deformed calcite marble: diffusion accommodated grain boundary sliding as a result
679 of subgrain rotation recrystallization. *Journal of Structural Geology*, 25(10), 1597-
680 1613.
- 681 Bhattacharyya, D. (1966). Orientation of mineral lineation along the flow direction in rocks.
682 *Tectonophysics*, 3(1), 29-33.
- 683 Bogard, D. D., & Johnson, P. (1983). Martian gases in an Antarctic meteorite? *Science*,
684 221(4611), 651-654.
- 685 Boiron, T., Bascou, J., Camps, P., Ferré, E., Maurice, C., Guy, B., Gerbe, M.-C., & Launeau,
686 P. (2013). Internal structure of basalt flows: insights from magnetic and
687 crystallographic fabrics of the La Palisse volcanics, French Massif Central.
688 *Geophysical Journal International*, 193(2), 585-602.
- 689 Borthwick, V. E. and Piazzolo S., 2010, Post-deformational annealing at the subgrain scale:
690 Temperature dependant behaviour revealed by in-situ heating experiments on
691 deformed single crystal halite, *Journal of structural Geology*, 32(7), 982-996.
- 692 Bridges, J. C., Hicks, L. J., & Treiman A. H., (2019), Carbonates on Mars in Volatiles in the
693 Martian Crust, 1st Edition, Eds Filiberto and Schwenzer, 426.
- 694 Bunch, T., & Reid, A. M. (1975). The nakhlites Part I: Petrography and mineral chemistry.
695 *Meteoritics & Planetary Science*, 10(4), 303-315.
- 696 Bunge, H.-J. (2013). *Texture analysis in materials science: mathematical methods*: Elsevier.
- 697 Changela, H., & Bridges, J. (2010). Alteration assemblages in the nakhlites: Variation with
698 depth on Mars. *Meteoritics & Planetary Science*, 45(12), 1847-1867.
- 699 Cohen, B., Mark, D. F., Cassata, W. S., Lee, M. R., Tomkinson, T., & Smith, C. L. (2017).
700 Taking the Pulse of Mars via ⁴⁰Ar/³⁹Ar Dating of a Plume-Fed Volcano. *Nature*
701 *communications*, 8(640).
- 702 Corrigan, C. M., Velbel, M. A., & Vicenzi, E. P. (2015). Modal abundances of pyroxene,
703 olivine, and mesostasis in nakhlites: Heterogeneity, variation, and implications for
704 nakhlite emplacement. *Meteoritics & Planetary Science*, 50(9), 1497-1511.
- 705 Day, J. M. D., Taylor, L. A., Floss, C., & McSween, H. Y. (2006). Petrology and chemistry
706 of MIL 03346 and its significance in understanding the petrogenesis of nakhlites on
707 Mars. *Meteoritics & Planetary Science*, 41(4), 581-606.

708 Fossen, H., & Tikoff, B. (1998). Extended models of transpression and transtension, and
709 application to tectonic settings. Geological Society, London, Special Publications,
710 135(1), 15-33.

711 Fritz, J., Artemieva, N., & Greshake, A. (2005). Ejection of Martian meteorites. *Meteoritics*
712 & *Planetary Science*, 40(9-10), 1393-1411.

713 George, R. P. (1978). Structural petrology of the Olympus ultramafic complex in the Troodos
714 ophiolite, Cyprus. *Geological Society of America Bulletin*, 89(6), 845-865.

715 Hallis, L., Taylor, G., Nagashima, K., Huss, G., Needham, A., Grady, M., & Franchi, I.
716 (2012). Hydrogen isotope analyses of alteration phases in the nakhlite martian
717 meteorites. *Geochimica et Cosmochimica Acta*, 97, 105-119.

718 Harvey, R. P., & McSween, H. Y. (1992). Petrogenesis of the nakhlite meteorites: Evidence
719 from cumulate mineral zoning. *Geochimica et Cosmochimica Acta*, 56(4), 1655-1663.

720 Hicks, L. J., Bridges, J. C., & Gurman, S.J. (2014) Ferric saponite and serpentine in the
721 nakhlite martian meteorites, *Geochimica et Cosmochimica Acta*, 136, 194-210.

722 Iezzi, G., & Ventura, G. (2002). Crystal fabric evolution in lava flows: results from numerical
723 simulations. *Earth and Planetary Science Letters*, 200(1-2), 33-46.

724 Ildefonse, B., Sokoutis, D., & Mancktelow, N. S. (1992). Mechanical interactions between
725 rigid particles in a deforming ductile matrix. Analogue experiments in simple shear
726 flow. *Journal of Structural Geology*, 14(10), 1253-1266.

727 Ismail, W. B., & Mainprice, D. (1998). An olivine fabric database: an overview of upper
728 mantle fabrics and seismic anisotropy. *Tectonophysics*, 296(1-2), 145-157.

729 Jackson, E. (1961). Primary textures and mineral associations in the ultramafic zone of the
730 Stillwater complex, Montana (2330-7102).

731 Ježek, J., Schulmann, K., & Segeth, K. (1996). Fabric evolution of rigid inclusions during
732 mixed coaxial and simple shear flows. *Tectonophysics*, 257(2-4), 203-221.

733 Johnson, A. M. (1970). Physical processes in geology: A method for interpretation of natural
734 phenomena; intrusions in igneous rocks, fractures, and folds, flow of debris and ice:
735 Freeman, Cooper.

736 Lentz, R. F., Taylor, G., & Treiman, A. (1999). Formation of a Martian pyroxenite: A
737 comparative study of the nakhlite meteorites and Theo's Flow. *Meteoritics &*
738 *Planetary Science*, 34(6), 919-932.

739 Merle, O. (1998). Internal strain within lava flows from analogue modelling. *Journal of*
740 *Volcanology and Geothermal Research*, 81(3-4), 189-206.

741 Mikouchi, T., Koizumi, E., Monkawa, A., Ueda, Y., & Miyamoto, M. (2003). Mineralogy
742 and petrology of Yamato 000593: Comparison with other Martian nakhlite meteorites.
743 *Antarctic Meteorite Research*, 16, 34-57.

744 Mikouchi, T., Makishima, J., Kurihara, T., Hoffmann, V., & Miyamoto, M. (2012). Relative
745 burial depth of nakhlites revisited. 43rd Lunar and Planetary Science Conference,
746 2363.

747 Nyquist, L., Bogard, D., Shih, C.-Y., Greshake, A., Stöffler, D., & Eugster, O. (2001). Ages
748 and geologic histories of Martian meteorites *Chronology and evolution of Mars* (pp.
749 105-164): Springer.

750 Passchier, C. (1982). Pseudotachylyte and the development of ultramylonite bands in the
751 Saint-Barthelemy Massif, French Pyrenees. *Journal of Structural Geology*, 4(1), 69-
752 79.

753 Paterson, S. R., Fowler Jr, T. K., Schmidt, K. L., Yoshinobu, A. S., Yuan, E. S., & Miller, R.
754 B. (1998). Interpreting magmatic fabric patterns in plutons. *Lithos*, 44(1-2), 53-82.

755 Peterson, D. W., Holcomb, R. T., Tilling, R. I., & Christiansen, R. L. (1994). Development of
756 lava tubes in the light of observations at Mauna Ulu, Kilauea Volcano, Hawaii.
757 *Bulletin of Volcanology*, 56(5), 343-360.

758 Piazzolo, S., Bons, P. D., Passchier, C.W., (2002), The influence of matrix rheology and
759 vorticity on fabric development of populations of rigid objects during plane strain
760 deformation, *Tectonophysics*, 351(4), 315-329.

761 Prior, D. J., Boyle, A. P., Brenker, F., Cheadle, M. C., Day, A., Lopez, G., Peruzzo, L., Potts,
762 G. J., Reddy, S., & Spiess, R. (1999). The application of electron backscatter
763 diffraction and orientation contrast imaging in the SEM to textural problems in rocks.
764 *American Mineralogist*, 84(11-12), 1741-1759.

765 Richter, F., Chaussidon, M., Mendybaev, R., & Kite, E. (2016). Reassessing the cooling rate
766 and geologic setting of Martian meteorites MIL 03346 and NWA 817. *Geochimica et*
767 *Cosmochimica Acta*, 182, 1-23.

768 Shelley, D. (1985). Determining paleo-flow directions from groundmass fabrics in the
769 Lyttelton radial dykes, New Zealand. *Journal of Volcanology and Geothermal*
770 *Research*, 25(1-2), 69-79.

771 Skemer, P., Katayama, I., Jiang, Z., & Karato, S.-i. (2005). The misorientation index:
772 Development of a new method for calculating the strength of lattice-preferred
773 orientation. *Tectonophysics*, 411(1-4), 157-167.

774 Tikoff, B., & Fossen, H. (1999). Three-dimensional reference deformations and strain facies.
775 *Journal of Structural Geology*, 21(11), 1497-1512.

776 Treiman, A. H. (2005). The nakhlite meteorites: Augite-rich igneous rocks from Mars.
777 *Chemie der Erde-Geochemistry*, 65(3), 203-270.

778 Udry, A., & Day, J. M. D. (2018). 1.34 billion-year-old magmatism on Mars evaluated from
779 the co-genetic nakhlite and chassignite meteorites. *Geochimica et Cosmochimica*
780 *Acta*, 238, 292-315.

781 Ventura, G., De Rosa, R., Colletta, E., & Mazzuoli, R. (1996). Deformation patterns in a
782 high-viscosity lava flow inferred from the crystal preferred orientation and
783 imbrication structures: an example from Salina (Aeolian Islands, southern Tyrrhenian
784 Sea, Italy). *Bulletin of Volcanology*, 57(7), 555-562.

785 Vollmer, F. W. (1990). An application of eigenvalue methods to structural domain analysis.
786 *Geological Society of America Bulletin*, 102(6), 786-791.

787 Wada, Y. (1992). Magma flow directions inferred from preferred orientations of phenocryst
788 in a composite feeder dike, Miyake-Jima, Japan. *Journal of Volcanology and*
789 *Geothermal Research*, 49(1-2), 119-126.

790 Watt, L. E., Bland, P. A., Prior, D. J., & Russell, S. S. (2006). Fabric analysis of Allende
791 matrix using EBSD. *Meteoritics & Planetary Science*, 41(7), 989-1001.

792

793

794

795

796

797

798

799

```

800 Supplementary materials
801 MATLAB MTEX codeline*
802 Set up
803 startup_mtex
804 Import ebsd data
805 Run and save
806 Copy crystallographic information from EBSD window.
807 cs_aug=crystalSymmetry('12/m1', [9.7381 8.8822 5.2821], [90,106.23,90]*degree, 'X||a*',
808 'Y||b*', 'Z||c', 'mineral', 'Augite')
809 J-Index
810 odf_aug=calcODF(ebsd('Augite').orientations)
811 J_aug=textureindex(odf_aug)
812 M-Index
813 [density_uniform,~]=calcAngleDistribution(cs_aug)
814 density_uniform=density_uniform/sum(density_uniform)
815 mdf=calcMDF(odf_aug)
816 [density_MDF,~]=calcAngleDistribution(mdf,'resolution',1*degree)
817 density_MDF=density_MDF/sum(density_MDF)
818 M_index=(sum((abs(density_MDF-density_uniform))/2))
819 PGR data
820 o=(ebsd('Augite').orientations)
821 v=o*Miller(1,0,0,cs_aug,'Augite','uvw') change miller to correct crystal axis
822 [x,y,z]=double(v)
823 OT=1./numel(x)*[x,y,z]*[x,y,z]
824 [Vec,Diagonal]=eig(OT)

```

```
825 value=diag(Diagonal)
826 [value,index]=sort(value,'descend')
827 vec1(1:3)=Vec(:,index(1))
828 vec2(1:3)=Vec(:,index(2))
829 vec3(1:3)=Vec(:,index(3))
830 NORM=value(1)+value(2)+value(3)
831 P100=(value(1)-value(2))/NORM
832 G100=(2.0*(value(2)-value(3)))/NORM
833 R100=(3.0*value(3))/NORM
834 PGR=P100+G100+R100
835
836 *note this codeline works for Augite. To adapt the code for another mineral phase replace
837 crystal data, the word Augite and associated abbreviations with the mineral of interest.
838
```